Journal of Power Sources 660 (2025) 238505

Contents lists available at ScienceDirect

Journal of Power Sources

journal homepage: www.elsevier.com/locate/jpowsour

Alginate-based separators for sustainable energy storage devices

Antonio De Marco [a], Giampaolo Lacarbonara [a,b,**], Mariangela Rea [a], Serena Tombolesi [a], Rossella Petruzzelli [a], Chiara Gualandi [a,b], Maria Letizia Focarete [a,b], Catia Arbizzani [a,b,*]

[a] Alma Mater Studiorum - University of Bologna, Dept. of Chemistry "Giacomo Ciamician", Via P. Gobetti 85, 40129, Bologna, Italy
[b] INSTM UdR of Bologna, University of Bologna, Via Gobetti 85, 40129, Bologna, Italy

HIGHLIGHTS

- Alginate-based separators made via a sustainable, water–ethanol-based process.
- Applicable in both lithium batteries and aqueous supercapacitors.
- High electrolyte affinity, good mechanical properties, and long-term stability.
- Long-term stability proven with >250,000 cycles in aqueous supercapacitors.

GRAPHICAL ABSTRACT

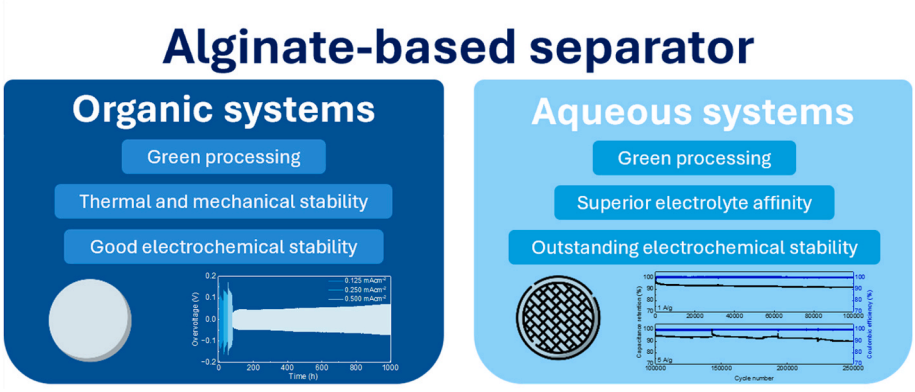

ARTICLE INFO

Keywords:
Alginate-based separator
Aqueous supercapacitor
Sodium alginate
Calcium alginate
Polyethylene oxide
Phase inversion

ABSTRACT

The separator is a crucial component of batteries, as it prevents electrical short circuits by acting as a physical barrier between anode and cathode. Nonetheless, it allows ion transport closing the circuit. Traditional polyolefin-based separators are widely used in lithium-ion technologies due to their affordability and chemical stability. However, their high stability results in high resistance to biodegradation. To address this issue, the adoption of biobased separators is necessary. In this work, three different alginate-based separators are proposed for application in both organic and aqueous systems. Sodium alginate and calcium alginate were selected as low-cost, biodegradable natural polymers with excellent thermal and chemical stability. A sustainable preparation route was designed based on the phase inversion technique, using water and ethanol as solvents. After assessing the materials thermal stability, physical insights were gained by evaluating the separators mechanical stability, morphology and affinity with both organic and aqueous electrolyte. Finally, electrochemical tests were performed in lithium metal cells, as well as in supercapacitor, to evaluate the performance of the alginate-based separators.

This article is part of a special issue entitled: In memory of Professor Bruno Scrosati published in Journal of Power Sources.

* Corresponding author. Alma Mater Studiorum - University of Bologna, Dept. of Chemistry "Giacomo Ciamician", Via P. Gobetti 85, 40129, Bologna, Italy
** Corresponding author.
E-mail addresses: giampaol.lacarbonar2@unibo.it (G. Lacarbonara), catia.arbizzani@unibo.it (C. Arbizzani).

https://doi.org/10.1016/j.jpowsour.2025.238505
Received 1 June 2025; Received in revised form 22 September 2025; Accepted 26 September 2025

1. Introduction

Rechargeable energy storage devices have had a profound impact on society due to their ability to reversibly store and deliver electrical energy. Since their invention, batteries have undergone significant changes in architecture, chemistry, and performance. Today, they play an even more critical role, driven by the growing adoption of renewable energy sources and the electrification of transport [1]. In a future with growing sustainable energy demands, electrochemical energy storage systems must be tailored to specific applications. This means adjusting the materials and structure to achieve desired performance characteristics. Since technical requirements, such as energy storage capacity, charge/discharge rate and lifespan, vary by application, different electrochemical storage systems are needed, such as batteries and supercapacitors [2]. When these devices operate with liquid electrolytes, separator is a key-component that ensures the physical separation between the electrodes, preventing short circuits while allowing ionic transport [3].

Although the separator is not an active part, its properties are crucial for the device stability and performance [4]. Its chemical and electrochemical stabilities are critical, as the separator must remain inert and not take part in any chemical or electrochemical reactions. Additionally, a good separator should show a high melt integrity temperature that is the temperature at which the material loses its dimensional stability [5]. Moreover, an ideal polymeric separator should also feature a "shutdown function", which is also related to the polymer melting temperature. From a morphological perspective, the separator should have an optimal thickness, typically around 10–25 μm: thinner separators have been studied for enhancing energy density but with an increased risk of punctures and short circuits. Conversely, thicker separators provide better mechanical strength and safety but have negative impact on energy density [6]. Mechanical properties, including tensile, tear, and puncture strength, are fundamental for withstanding physical stress from external compression and electrode expansion. As an example, puncture strength is critical for resisting dendrite penetration when the separator is applied to metal batteries [7].

The separator must absorb sufficient electrolyte to minimize ionic resistance and maintain conductivity during cell operation, achieving values between $1{\cdot}10^{-3}$ and $1{\cdot}10^{-1}$ S cm^{-1}, close to the ionic conductivity of the bulk electrolyte. As the separator must host the electrolyte, the porosity is another key property. On one hand, higher porosity improves electrolyte uptake and ionic conduction but weakens mechanical strength, on the other hand lower porosity enhances mechanical properties but limits electrolyte uptake [8]. The MacMullin number gives an estimation of the ionic transport between the two electrodes. A good separator has a MacMullin number around 8 [4,9,10].

As the separator accounts for about 20 % of a battery's total cost with manufacturing being the primary expense, efficient production methods are key factors to reducing overall costs [11]. State-of-art polymer separators, such as those made of single or multiple layers of polyethylene (PE) or polypropylene (PP), are widely used in commercial lithium-ion batteries (LIBs) due to their consolidated manufacturing, easy handling and low cost [12]. While these materials are often referred to as microporous in battery literature, their pore sizes are more accurately classified as macroporous or mesoporous according to IUPAC definitions. Multilayer systems offer enhanced properties by combining materials with complementary functions. For example, PE-PP bilayer or trilayer systems improve safety by preventing thermal runaway in case of short circuits. In such a system, the PE layer melts at its melting temperature (135 °C), blocking ion transport, while the PP layer, having higher melting point, keeps structural integrity. Hence, material choice and separator manufacturing are fundamental for developing separators with the desired properties and moderate cost [3,13]. Owing to its many advantages, phase inversion is a widely employed technique for the fabrication of polymeric membranes. In this process, the polymer transition from solution to solid phase occurs in a controlled manner. A polymeric solution is spread onto a suitable substrate and then submerged in a coagulation bath containing a non-solvent. The precipitation of the polymer occurs due to the exchange of the solvent with the non-solvent. The resulting membrane structure is determined by the interplay between mass transfer and phase separation during the process [9,14].

One of the key benefits of the phase inversion method is the ability to achieve precise control over the pore size, morphology, and overall porosity of the separators. This is carried out by fine-tuning parameters such as polymer concentration, solvent type, and non-solvent composition, potentially enabling a balance between transport properties and mechanical stability. Furthermore, the method shows remarkable versatility, as it supports the use of a broad spectrum of polymers. This adaptability helps the customization of separator properties to meet the requirements of various applications, such as in batteries and supercapacitors. The phase inversion process is also highly scalable, making it well-suited for industrial production [15,16].

From the perspective of material selection, traditional synthetic separators such as PE and PP offer excellent electrochemical and mechanical properties and are typically recovered during battery recycling, thus not contributing directly to plastic pollution. However, they are still derived from fossil resources and are not biodegradable. In contrast, biobased and biodegradable materials, while requiring a balanced assessment of their performance, may offer additional advantages in the context of battery end-of-life management. If the separator is incorporated into the black mass, the use of biodegradable polymers can simplify downstream recycling steps by reducing the need for aggressive treatments aimed at removing persistent synthetic components. [17]. Under the bioeconomy concept, renewable resources have been used to develop green alternatives like bio-based polymeric membranes. These membranes, produced from natural polymers derived from plants, animals, or marine waste materials, align with sustainability goals [18].

Considering these alternatives, new types of separators composed of biopolymers and water-processable polymers are increasingly being investigated as sustainable options. Carboxylated cellulose [19], carrageenan [20], sodium alginate [21], chitin [22], chitosan [23], and many others have been proposed as biopolymers for sustainable separators. Sodium alginate (SA), a linear polysaccharide composed of 1, 4-β-D-mannuronic and α-L-guluronic acids, is a cell wall component of brown algae. Its solubility in water makes it suitable for aqueous processing [24]. SA has already proven its appeal in battery research, as it has been widely applied as binder in the development of sustainable anodes [25–27], cathodes [28,29] and separators [30]. Additionally, alginates forms a gel in the presence of calcium ions, paving the way also to its applicability in aqueous systems. Calcium alginate (CA) demonstrated, indeed, excellent thermal stability and wettability.

This work explores the feasibility of alginate-based composites as green separators for both organic and aqueous devices, introducing two innovative designs developed through an eco-friendly process. The first combines SA with polyethylene oxide (PEO), a well-known and widely used polymer material in battery research, to enhance affinity with the organic liquid electrolytes used in lithium batteries. The second design uses CA and PEO, integrated with an electrospun polyvinylidene fluoride (PVDF)/PEO scaffold. The supramolecular crosslinking of SA with calcium ions prevents dissolution in aqueous electrolyte, while the scaffold enhances the mechanical properties. The membranes are prepared via phase inversion using water as a solvent and ethanol as an antisolvent, paving the way for sustainable and eco-friendly production. Each separator, according to its properties, has been tested in organic lithium batteries or aqueous supercapacitors.

2. Experimental section

2.1. Materials

The materials used for the preparation of the separators were SA

(Sigma Aldrich, Merck Life Science S.r.l., Milan, Italy, purity), PEO (5000000 Da, Merck Life Science S.r.l., Milan, Italy), calcium chloride ($CaCl_2$, ≥99 %, Sigma Aldrich, Merck Life Science S.r.l., Milan, Italy), PVDF/PEO electrospun scaffold (PVDF6020/ PEO100 90/10 w%) from a 15 % w/V dimethylformamide (DMF) solution [31], and ethanol (EtOH, absolute,>99.8 % Sigma Aldrich, Merck Life Science S.r.l., Milan, Italy). Freeze drying was performed during the processing of the materials with an Alpha 1–2 LDplus (CHRIST) freeze-dryer at −60 °C for 6 h. Commercial three-layer PP/PE/PP membranes (Celgard LLC, Charlotte, North Carolina, USA), Celgard® 2300 (thickness: 25.4 μm, Gurley 24 s) and Celgard® 3419s (thickness: 25 μm, Gurley 40 s, referred as Celgard®aq) were used as benchmarks for measurements in organic and aqueous based electrolyte, respectively.

For the electrochemical characterizations in organic electrolyte, lithium (Li metal ribbon, 99,9 %, 0.75 mm thick, Sigma Aldrich, Merck Life Science S.r.l., Milan, Italy) and lithium iron phosphate (LFP, NEI Corporation, ≈ 88 % active material, areal capacity ≈ 1.25 mAh cm^{-2}) were use as electrodes. The electrolyte 1M $LiPF_6$ in ethylene carbonate (EC): dimethyl carbonate (DMC) in a 1:1 v/v (LP30, Solvionic, Toulouse, France) was used in Li//Li cells and 1M $LiPF_6$ in EC:DMC 1:1 v/v + 2 % wt vinylene carbonate (Solvionic, Toulouse, France) + 10 wt% fluoroethylene carbonate (Solvionic, Toulouse, France) was used in Li//LFP cells. For the test in aqueous electrolyte, a supercapacitor with capacitive electrodes was assembled. Activated carbon (AC, Picactif BP10 PICA USA, Inc. Columbus, Ohio, United States), 5 wt% of conductive additive (Super C45, Imerys Graphite & Carbon Switzerland SA, Bodio, Switzerland) and 5 wt% of polytetrafluoroethylene (PTFE) from aqueous suspension (Dupont De Nemour Netherlands B.V., Dordrecht, Netherlands, 60 wt%) were used to prepare AC electrodes by grinding the solids in a mortar and adding stepwise 100 μL of EtOH. Self-standing electrodes were prepared following the procedure described in Ref. [32]. Sodium nitrate ($NaNO_3$, ≥99 %, Sigma Aldrich, Merck Life Science S.r.l., Milan, Italy) was used for the preparation of a solution 5M of $NaNO_3$ in MilliQ water.

2.2. Physicochemical characterization

Thermogravimetric analysis (TGA) was carried out with a Q50 TA Instrument (Waters S.p.A., Milan, Italy). About 5–10 mg of sample were placed in an alumina pan and heated at 5 °C min^{-1} from 30 °C to 800 °C, under argon (Ar) atmosphere. Differential scanning calorimetry (DSC) was carried out using a Q2000 DSC apparatus (TA Instruments, Waters S.p.A., Milan, Italy) equipped with a refrigerated cooling system (RCS90). Analyses were performed on 4–6 mg samples that were previously placed inside aluminium pans. Such samples were subjected to different calorimetric scans: two heating scans at a rate of 10 °C min^{-1} up to 150 °C alternated with a cooling scan at a rate of 10 °C min^{-1} to −90 °C.

The electrolyte uptake of the separators was evaluated using the following procedure. First, the separator was kept under vacuum at 50 °C for 12 h. After this step, the sample was weighed, and its mass recorded. Subsequently, the sample was immersed in 500 μL of the electrolyte solution for 24 h. After the immersion period, the sample was weighed again. To minimize solvent loss due to the evaporation during the weighing process, the second measurement was performed inside a closed container. Finally, the electrolyte uptake was calculated using equation (1).

$$\text{Electrolyte uptake } (\%) = \frac{W_{wet} - W_{dried}}{W_{dried}} \cdot 100 \quad (1)$$

In the calculation, w_{wet} stands for the weight of the wet sample, and w_{dried} denotes the weight of the dry sample. The electrolyte uptake was assessed for the two different electrolytes at least in triplicate.

2.3. Mechanical characterization

The mechanical tensile characterization of the samples was carried out using a material testing machine (Mod. 4465, Instron, Norwood, USA) equipped with a 100 N load cell (Instron, Norwood, USA). The tests were carried out in displacement control mode and the acquired load-displacement curves were converted into stress-strain curves. The mechanical data are provided as mean ± standard deviation. Five replicates were tested for each mat and subjected to a deformation rate of 5 mm min^{-1}. The rheological properties of the CA/PEO and CA/PEO without the PVDF/PEO mat hydrogels systems were evaluated using an MCR 102 parallel-plate rheometer (Anton Paar, Graz, Austria) equipped with a 25 mm diameter plate (PP-25) and a gap setting of 0.7 ± 0.2 mm. Samples were applied onto the rheometer's lower plate using a spatula, after which the upper plate was lowered until it made contact with the sample surface. Excess material was carefully removed, and the surrounding trap was filled with distilled water to minimize evaporation. An oscillatory amplitude sweep test was then performed at 25 °C to determine the storage modulus (G'), loss modulus (G"), cross-over point (G' = G"), and linear viscoelastic range (LVER). The test was conducted over a shear strain amplitude range of 0.01 %–100 % at a constant frequency of 5 rad s^{-1}. Data are presented as mean ± standard deviation (SD), with n = 2.

2.4. Morphological characterization

Scanning electron microscopy (SEM) images were obtained using a ZEISS Crossbeam 550 (Carl Zeiss SMT GmbH, Oberkochen, Germany) equipped with a Gemini II field emission (FE-SEM) column. Prior to SEM analysis, the samples were sputtered with gold using an Edwards S150B sputter coater, with a gold target and an applied current of 30 mA for 2 min. SEM images of the calcium alginate-based system were obtained from freeze-dried samples. The freeze-drying step was necessary to prevent structural modifications caused by the strong drying conditions needed to prepare samples for SEM analysis.

2.5. Electrochemical characterization

Electrochemical characterizations were carried out in T-shaped Teflon cells (BOLA, Bohlender GmbH, Grünsfeld, Germany) that were assembled in glove box (Mbraun Labmaster SP) in Ar inert atmosphere (O_2 < 0.1 ppm and H_2O < 0.1 ppm) using stainless steel (SS) pistons. Characterization in aqueous electrolyte was conducted in an ECC-Aqu Electrochemical Cell (EL-Cell GmbH, Hamburg, Germany) with gold current collector. The electrochemical tests have been performed with a BioLogic VSP potentiostat/galvanostat (BioLogic SAS, Seyssinet-Pariset, France). Potentiostatic electrochemical impedance spectroscopy (PEIS) experiments for the determination of the MacMullin number have been conducted in the frequency range 100 kHz–10 kHz, with a perturbation amplitude of 10 mV around open circuit voltage (OCV) and recording 10 points per decade. In particular, the PEIS spectrum of a cell with blocking SS electrodes and separators soaked in LP30 was recorded. The ionic resistance of the electrolyte-soaked separator was found by a linear fit of the results in the high-frequency region and identifying the intercept with the Z_{re} axis. The MacMullin number N_M was then calculated using equation (2).

$$N_M = \frac{\rho_{(electroyte+separator)}}{\rho_{electroyte}} \quad (2)$$

here $\rho_{electrolyte\ +\ separator}$ is the resistivity of the electrolyte-soaked separator and $\rho_{electrolyte}$ is the resistivity of the electrolyte. For the tests in organic electrolyte, SA/PEO (10 mm diameter, 50 μm thick) was dried at 50 °C under vacuum for 12 h and stored in glove box. CA/PEO (10 mm diameter, 95 μm thick) was stored in the glove box immediately after the freeze drying to avoid water uptake. Li//Li symmetric cells

were assembled using SA/PEO and CA/PEO soaked in LP30 for 2 h and Li electrodes (9 mm diameter). The total amount of electrolyte added is 800 µL. These cells were characterized at 30 °C using the following test protocol: 25 deposition/stripping cycles at 0.125 mA cm^{-2}; 25 deposition/stripping cycles at 0.250 mA cm^{-2}; 25 deposition/stripping cycles at 0.500 mA cm^{-2}; 925 deposition/stripping cycles at 0.125 mA cm^{-2}; each cycle is composed by 30 min deposition and 30 min stripping.

Moreover, further electrochemical analysis was performed for evaluating the SA/PEO separator. ECC.Std cells (EL-Cell GmbH, Hamburg, Germany) were assembled in an argon-filled glove box. The working electrode (WE) consisted of LFP (9 mm diameter), while lithium metal disk (0.75 mm thick, 16 mm diameter) was used as counter electrode (CE). The SA/PEO separator (19 mm diameter) was vacuum-dried at 110 °C for 10 h prior to cell assembly [21]. The electrochemical test was conducted at 30 °C controlled temperature. Galvanostatic charge-discharge with potential limitation (GCPL) cycling was performed with a voltage window of 2.5–3.8 V vs Li/Li^+. As a first step, the cells underwent an open-circuit voltage (OCV) rest for 5 h to allow cell stabilization. Subsequently, three formation cycles were carried out at a C-rate of C/10 (0.080 mA), followed by an extended cycling at C/2 (0.397 mA).

For the test in aqueous electrolyte, CA/PEOaq (18 mm diameter, 300 µm thick) was soaked in $NaNO_3$ 5M for 10 min and symmetric cells were assembled with AC electrodes (18 mm diameter, 9.4 mg cm^{-2}). No further electrolyte was added. The symmetric supercapacitor was characterized as follows: 4 cyclic voltammetries (CVs) at each different scan rates (5, 10, 20, 50, 100 mV s^{-1}); 100000 galvanostatic charge and discharge cycles in the voltage range of 0 V and 1.4 V at 1 A g^{-1} (18.9 mA cm^{-2}), 100000 galvanostatic charge and discharge cycles at 5 A g^{-1} (94.5 mA cm^{-2}) in the same voltage range. The specific currents were referred to the mass of both electrodes.

3. Results and discussion

3.1. Separator preparation

The preparation procedure (Fig. 1) has been designed to employ sustainable solvents and to precisely control critical properties of the separator, including thickness and porosity. SA was selected as a biopolymer soluble in water that can be precipitated in ethanol, a green antisolvent, ensuring an environmentally friendly process. PEO, while not precipitating in ethanol in its pure form, was included in the blend to enhance affinity with alkyl carbonate solvents and promote ion conduction. Notably, PEO precipitates when blended with the SA, facilitating the formation of a porous structure. For the preparation, a polymer mixture (30 mg) with a SA:PEO ratio of 7:3 is dissolved in 2 mL of distilled water under magnetic stirring for 16 h. The resulting transparent solution is then cast onto Teflon moulds. From this solution, three different separators were prepared. The first separator is obtained by immersing the mould in an EtOH bath for 45 min to induce phase inversion. Afterwards, the wet film is hot-pressed at 90 °C for 30 min to evaporate the liquid, resulting in a solid, dried separator composed of SA and PEO (referred to as the SA/PEO separator). For the second separator, a slightly modified process is followed. After 15 min of phase inversion in EtOH, a PVDF/PEO scaffold is added to the mould. The resulting porous film is then crosslinked with a $CaCl_2$ 5 % w/w aqueous solution, forming a gel-like structure. The gel is then carefully washed with ethanol and Milli-Q water to eliminate residues of $CaCl_2$ and NaCl. This separator, primarily composed of CA and PEO, is designed for testing in aqueous systems and referred to as CA/PEOaq separator. The third separator is derived from the second one through freeze-drying. This step yields a CA/PEO separator that must be stored under dry conditions given that the freeze drying has completely removed water in the system.

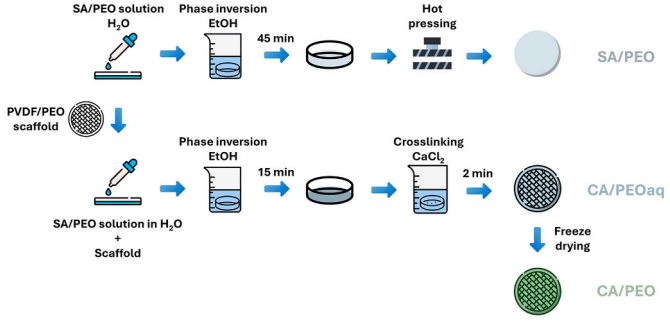

Fig. 1. SA/PEO, CA/PEOaq and CA/PEO separator preparation.

3.2. Thermal characterization

Thermogravimetric analysis was used to determine the degradation steps of the separator and to quantify the presence of PEO in the membrane after processing in a solvent in which PEO is soluble in its pure form. Thermogravimetric curves of SA/PEO separator and of the individual components are reported in Fig. 2. The SA/PEO separator shows a two-step degradation. The first step at 240 °C is associated with the degradation of the SA, which corresponds to the 28.8 % of weight loss, while the second step occurs at 387 °C and is associated with the cleavage of the PEO main chain, resulting in a weight loss accounting for the 22.8 % of the total. Comparing the PEO weight loss in the SA/PEO separator with the loss in the analysis of the PEO powder (91.0 %), it can be confirmed that the PEO accounts for 30 % of the total weight of the separator (also considering the water contribution). This shows that, even if the PEO is partially soluble in EtOH, during the phase inversion, there is no polymer loss during the preparation. The single thermogravimetric curves are reported in Fig. S1.

The TGA curve of CA/PEO is reported in Fig. 2c and d. It shows a three-step degradation: the first degradation step is associated with the breakdown of CA at 240 °C, resulting in a 14.1 % weight loss. CA shows a degradation profile characterized by a single main step with two distinct peaks in the dTGA, both around 250 °C, as the chain segments involved in the egg-box structures tend to degrade at higher temperatures. The second weight loss (14.8 %) at 387 °C corresponds to the degradation of PEO. The third and final degradation step (15.3 %) at 473 °C is related to the scaffold, specifically to the degradation of PVDF. In this case, the determination of the composition is more challenging due to the presence of the scaffold. It is important to note that, under inert atmosphere conditions, thermal degradation of polymers begins with chain scission events that do not immediately lead to weight loss detectable by TGA. Therefore, the initial stages of polymer degradation occur prior to the observable mass loss, and TGA curves primarily reflect the formation of volatile decomposition products rather than the onset of degradation itself. In addition, it should be noted that although PEO is known to undergo severe chain scissions and a marked decrease of its average molecular weight even under mild stirring conditions [33], in our case this aspect was carefully considered. The thermogravimetric curves of PEO powder and of the PEO in the separator show very similar degradation temperatures, supporting the hypothesis that the gentle stirring applied during membrane preparation did not induce significant chain scission or polymer degradation.

Samples were analyzed by DSC to investigate the effects of the obtained systems on PEO crystallization. Fig. 3a reports a comparison of the first heating scan of SA/PEO, SA and PEO samples. A narrow melting peak characterizes pure PEO at a maximum temperature of 68 °C, while a broad endothermic peak around 100 °C is present for SA sample, corresponding to the evaporation of water molecules entrapped into its network. SA/PEO curve includes both the peaks observed for the two single starting materials. The values of glass transition temperature (T_g) and melting enthalpy (ΔH_m) are reported in Table S1. The ΔH_m of SA/PEO is much smaller than that of PEO, indicating the lower amount of

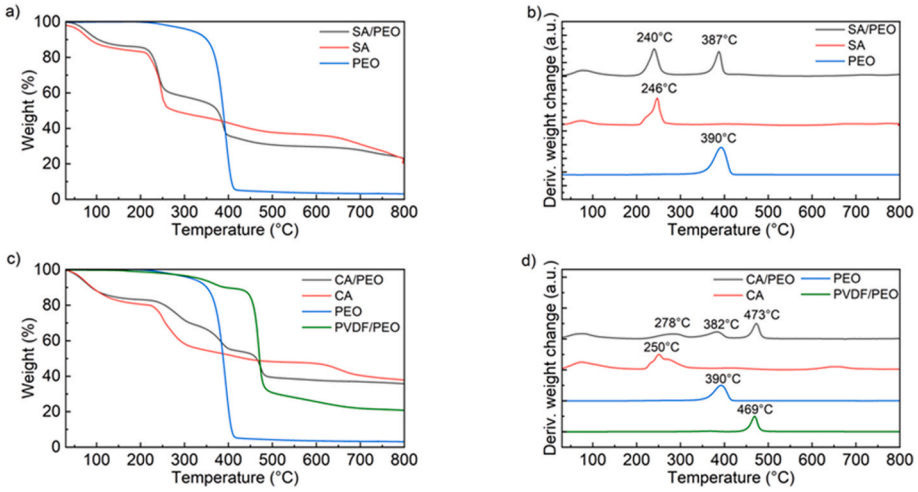

Fig. 2. a) TGA curves and b) dTGA curves of the SA/PEO separator and of the individual components; c) TGA curves and d) dTGA of the CA/PEO separator and of the individual components.

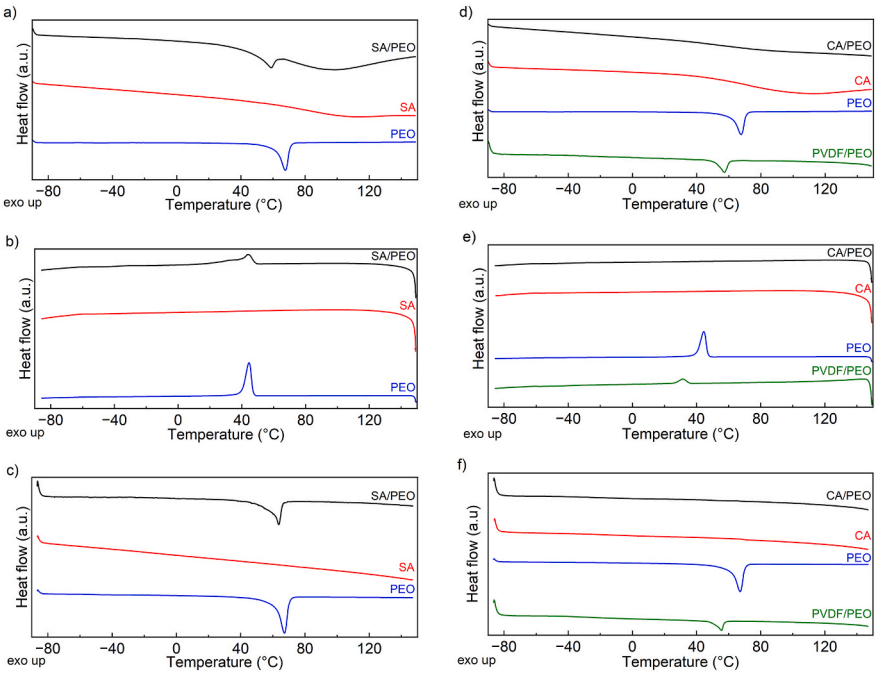

Fig. 3. DSC analysis of SA/PEO, SA, PEO samples: (a) first heating scan, (b) cooling scan and (c) second heating scan; DSC analysis of CA/PEO, CA, PEO, PVDF/PEO samples: (d) first heating scan, (e) cooling scan, and (f) second heating scan.

crystalline phase in the sample, linked with the presence of the amorphous SA. Indeed, from the overlay of the cooling scan (Fig. 3b), no crystallization peaks are observable for SA, while a narrow peak characterizes PEO sample and a broad one is present in SA/PEO sample. This step confirms the fact that the presence of SA hinders PEO crystallization. In fact, ΔH_c of SA/PEO is much smaller than that of PEO (Table S1). The second heating scan of PEO sample is almost overlapping the first one, while the one of SA does not present anymore the broad endothermic peak associated with the presence of water molecules, which were eliminated during the first scan (Fig. 3c). An endothermic step is visible at around −20 °C, corresponding to the T_g and another one at 67 °C in SA curve. Also, the SA/PEO curve does not include anymore the peak associated with water evaporation, so it is possible to evaluate more precisely the ΔH_m. More specifically, the percentage of crystallinity (X_c%) of PEO was calculated according to equation (3).

$$X_C\% = \frac{\Delta H_m}{\Delta H^0_{100\%}} \cdot 100 \quad (3)$$

where $\Delta H^0_{100\ \%}$ corresponds to the heat enthalpy of 100 % crystalline PEO melting, that is 196.4 J g^{-1} [34]. X_c% is equal to 67 % for PEO, and 9 % for SA/PEO sample.

Similarly, CA, CA/PEO, PEO, PVDF/PEO are compared in Fig. 3d–f. CA curves are similar to those of SA, no differences are highlighted, and the sample is completely amorphous since no melting or crystallization peaks are evident. From PVDF/PEO first heating scan curve, it can be deduced that also PVDF hinders PEO crystallization, since ΔH_m is much lower than that of pure PEO (Table S1). The crystallization peak is less intense than that of pure PEO and occurs at a lower temperature (Table S1), evidencing a slower crystallization kinetic and lower amount of crystalline phase than PEO. The X_c% of PVDF/PEO is 2.7 %. Finally,

CA/PEO first heating scan reveals two T_g values: one at −44 °C, corresponding to that of PEO, and another at −22 °C, attributed to CA. These are followed by a broad endothermic peak related to the evaporation of residual water. No crystallization is detected during the cooling scan, indicating a predominantly amorphous system. In the second heating scan, T_g values of −40 °C (PEO) and −22 °C (CA) are again observed. The slight increase in PEO T_g compared to the neat polymer (−54 °C) suggests intermolecular interactions within the blend. An endothermic event at 48 °C is likely associated with the melting of low-crystalline PEO. Finally, a transition at 67 °C may correspond to the melting of PEO/PVDF mixed domains, where the presence of PEO acts as a plasticizer, lowering the typical melting point of PVDF (around 160–170 °C). The DSC curves of single components are reported in Fig. S2.

3.3. Mechanical characterization

The mechanical properties of the prepared samples were assessed using tensile stress–strain tests for the dry specimens and amplitude sweep rheological analyses for the hydrated ones. Fig. 4a and Table 1 display the representative stress–strain curves and the corresponding mechanical parameters, respectively. The SA/PEO system (Fig. 4a, black curve) shows a Young's modulus (E) similar to that of plain PVDF/PEO (Fig. S3), but significantly lower σ_b and ε_b values, resulting in increased brittleness and reduced flexibility. On the other hand, the CA/PEO blend (red curve) shows the lowest values for E, σ_b, and ε_b, suggesting a weak and relatively soft material. The gradual, flattened shape of the stress–strain curve reflects low stiffness and limited elasticity, likely due to the more amorphous and less organized structure of CA compared to the other systems. Additionally, the reduced mechanical performance may be attributed to poor intermolecular interactions and limited crosslinking density, potentially caused by processing factors such as inhomogeneous distribution after lyophilization. It must be considered that the mechanical properties of SA/PEO are also influenced by the presence of PEO crystal domains which tend to make the structure stiffer, an effect that is expected to be weakened at $T > T_m$. Conversely, this effect is not present in CA/PEO systems since no PEO crystallinity has been observed in DSC analysis.

Fig. 4b shows the amplitude sweep analysis of the CA/PEO hydrogel, both without and with the incorporation of the PVDF/PEO mat. Corresponding values of storage modulus (G'), loss modulus (G"), linear viscoelastic range (LVER), and cross-over points are summarized in Table 2. While the moduli of the two systems are nearly unchanged, the addition of the PVDF/PEO mat results in an extended LVER and shifts the cross-over point to higher shear strain values compared to the CA/PEO sample alone. This behaviour suggests that the mat slightly softens the hydrogel network, potentially enhancing flexibility, likely due to a reduction in crosslinking density or weaker interfacial adhesion between the hydrogel and the mat. Overall, the mechanical performance of the hydrated CA/PEO system appears suitable for applications that demand structural resilience and flexibility, such as flexible supercapacitor.

Table 1
Young's modulus (E), stress at break (σ_b), and deformation at break (ε_b) of the SA/PEO, CA/PEO and PVDF/PEO samples evaluated by stress-strain tests.

Sample	E (MPa)	σ_b (MPa)	ε_b (%)
SA/PEO	11.8 ± 0.1	18 ± 7	1.6 ± 0.9
CA/PEO	1.422 ± 0.005	4 ± 1	5.2 ± 0.1

Table 2
G′ and G″ values, LVER% and cross-over point (%) of CA/PEO hydrogel without and with the PVDF/PEO mat support.

Sample	G' (Pa)	G" (Pa)	LVER (%)	Cross-over point (%)
CA/PEO (no mat)	$5.4{\cdot}10^3 \pm 0.4{\cdot}10^3$	$1.12{\cdot}10^3 \pm 0.08{\cdot}10^3$	0.04	0.80
CA/PEO (mat)	$4.43{\cdot}10^3 \pm 0.96{\cdot}10^3$	$0.8{\cdot}10^3 \pm 0.2{\cdot}10^3$	0.06	1.84

3.4. Separator morphology and electrolyte compatibility

The morphology of the separator was evaluated using SEM, which are reported in Fig. 5. The SA/PEO separator (Fig. 5a and d) exhibits a relatively homogeneous surface with a compact morphology. At high magnification, few pores are evident, with dimensions ranging between 20 and 100 nm. This structure enhances mechanical stability and suggests a dense material with low porosity, potentially limiting its electrolyte-absorbing capability.

The CA/PEO system, obtained by crosslinking on the PVDF scaffold, exhibits a different morphology on the upper (Fig. 5b and e) and lower (Fig. 5c and f) sides of the membrane, with the lower side being in direct contact with the scaffold. The upper side of the membrane displays a three-dimensional network with interconnected pores. This significantly highly porous structure, with pore sizes in the range of hundreds of nanometres, could enhance electrolyte absorption and reduce the MacMullin number. Micrographs of the lower part of the membrane show that the mat nanofibers are homogeneously embedded within the polymer structure without altering their morphology (pristine PVDF fibres visible in Fig. S4a and b). Cross-sectional images allowed us to estimate the thickness of the separators (Fig. S4c and d), which are approximately 10 μm and 40 μm for the SA/PEO and CA/PEO systems, respectively.

The uptake of LP30 was measured for the SA/PEO separator, the CA/PEO separator, and commercial Celgard® 2300. Instead, the uptake of a 5 M $NaNO_3$ aqueous solution was evaluated for the CA/PEO aqueous separator and Celgard®aq. As shown in Fig. 6a, when using LP30 as the electrolyte, the SA/PEO separator shows a lower affinity for the electrolyte compared to commercial Celgard®2300. This could be related to the less porous structure of this membrane as shown in SEM images. Hence, the proper wetting of the separator is necessary before performing any electrochemical characterization. Conversely, the CA/PEO separator exhibits a higher electrolyte uptake, which can be attributed to its egg-box, highly porous structure that enables higher electrolyte

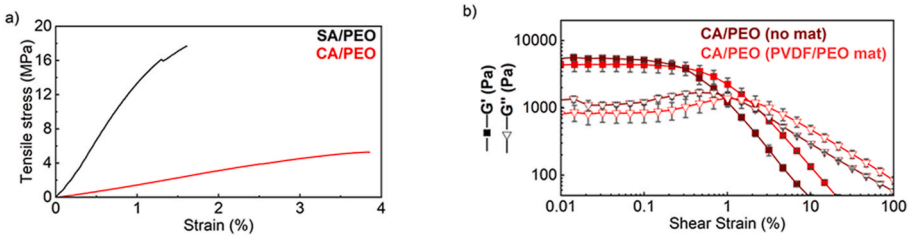

Fig. 4. Mechanical characterization: (a) Representative tensile stress-strain test of SA/PEO (black curve) and CA/PEO (red curve); (b) rheological amplitude sweep test of CA/PEO hydrogel system without PVDF/PEO mat (dark red curve) and of CA/PEO hydrogel system with PVDF/PEO mat support (red curve). (For interpretation of the references to colour in this figure legend, the reader is referred to the Web version of this article.)

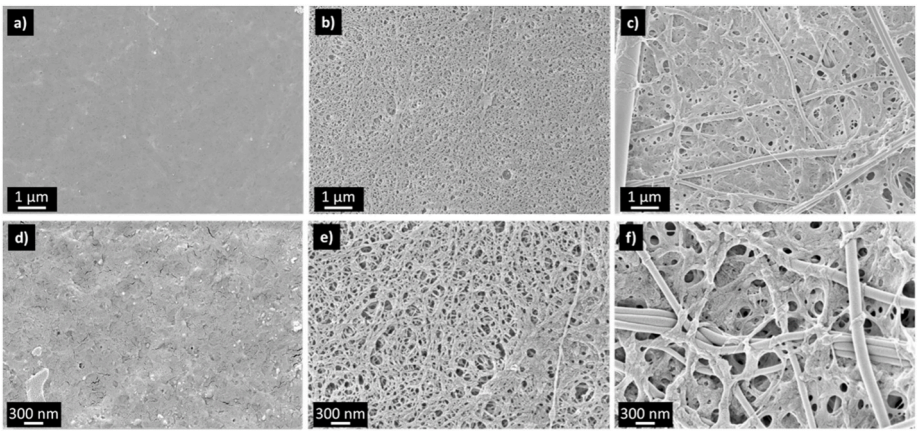

Fig. 5. SEM images of SA/PEO separator (a, d), of the upper side of the CA/PEO separator (b, e), and of the lower side of the CA/PEO separator (c, f).

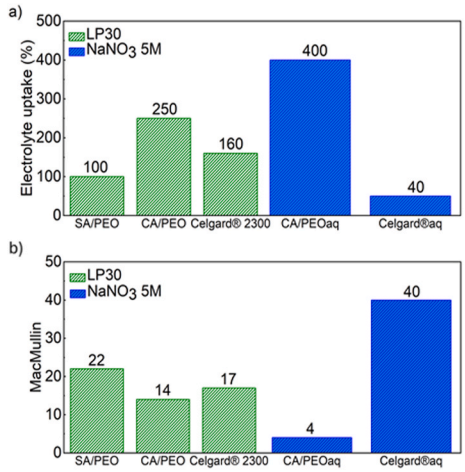

Fig. 6. LP30 (green) and $NaNO_3$ 5M (blue) electrolyte uptake (a) and N_M number (b) of different separators. (For interpretation of the references to colour in this figure legend, the reader is referred to the Web version of this article.)

accommodation compared to SA/PEO. This behaviour is confirmed when measuring the uptake of an aqueous electrolyte, where the CA/PEO separator shows an even greater affinity, forming a gel-like structure. Further contribution of the separators to the ionic resistance was estimated in both organic and aqueous electrolytes by PEIS spectra of a cell (Fig. S5a and S5b) with blocking stainless steel electrodes. The resistivity (ρ) and N_M numbers were obtained and reported in Table S2. Resistivity values of the system using the Celgard®2300 separator and of the bare LP30 electrolyte derive from Ref. [8]. The N_M numbers reported in Fig. 6b indicate that, when LP30 is used, the ionic transport using SA/PEO separator is less efficient than through Celgard®2300. Conversely, CA/PEO has a lower N_M that correlates with improved Li^+ ion conduction in the system. In the aqueous systems, CA/PEOaq exhibits an excellent N_M, particularly when compared to that of Celgard®aq. These results are consistent with the electrolyte uptake and DSC results previously reported. Indeed, since the crystal phase of PEO is no longer present in the CA/PEO separator, ionic transport through the separator is expected to be faster with respect to a system as SA/PEO, where the crystallinity can partially hinder it. Additionally, N_M results are further supported by SEM images where the higher porosity of the CA /PEO system, both in pore density and size, may lead to better electrochemical behaviour.

Although the electrolyte uptake and the N_M are both parameters influenced by the separator's ability to absorb and transport ionic species, their relationship is not directly proportional. In general, a higher electrolyte uptake tends to reduce the ionic resistance across the membrane, leading to a lower N_M. However, this inverse trend is not sufficient to establish a reliable correlation, as N_M also depends on other structural and functional factors such as tortuosity, pore interconnectivity, and the effective ionic mobility within the confined polymer–electrolyte environment. Therefore, while electrolyte uptake gives a first qualitative indication of separator wettability, N_M provides a more comprehensive insight into ionic transport and cannot be correlated to uptake alone.

3.5. Electrochemical characterization

Fig. 7a shows the deposition-stripping cycles at different current densities using the SA/PEO separator. The SA/PEO separator exhibited a stable behaviour as no short circuit events were observed even at higher current density. At long operation times, the SA/PEO cells showed an increasing overpotential suggesting the accumulation of dead lithium [35]. It must be noted that the CA/PEO system, despite exhibiting lower stability at higher currents, shows signs of self-healing. Indeed, when the current was reduced 0.125 mA/cm^2 the system regained stability (Fig. S6). Additionally, the advantage of using the CA/PEO separator over the SA/PEO consists in its lower overvoltage during cycling, despite being thicker. This observation aligns with the smaller N_M of the CA/PEO with respect to the SA/PEO separator.

Preliminarily, the performance of SA/PEO was also assessed by testing it in Li//LFP cell. Fig. 7b shows the charge/discharge profiles of the LFP electrode at two C-rates, C/10 (in black) and C/2 (in red). At C/10, the cell exhibits a well-defined voltage plateau around 3.4 V, which is characteristic of the two-phase reaction between $FePO_4$ and $LiFePO_4$ and delivers a relatively high discharge capacity (158.7 mAh g^{-1}). Upon increasing the C-rate to C/2, the cell undergoes a slight decrease in discharge capacity (147.8 mAh g^{-1}). Moreover, a moderate shift of the voltage profiles towards higher potentials characterized C/2 profile, which can be attributed to an increased overpotential. The performance of the Li//LFP cell in terms of capacity retention are not yet satisfactory and deserves deeper investigations (Fig. S7).

On the contrary, outstanding results were achieved with CA/PEOaq in aqueous devices. A symmetric supercapacitor was assembled to evaluate the applicability of an alginate-based system in an aqueous electrolyte. Thanks to supramolecular crosslinking, the CA/PEOaq separator is insoluble in aqueous media, and the high hydrophilicity of its components results in strong affinity with the electrolyte, as shown in Fig. 6. The cyclic voltammograms recorded between 0 and 1.4 V (Fig. S8) exhibit a typical box-like shape, without any clear degradation of the electrolyte-separator system.

Galvanostatic charge-discharge tests at 1 and 5 A g^{-1} confirmed the

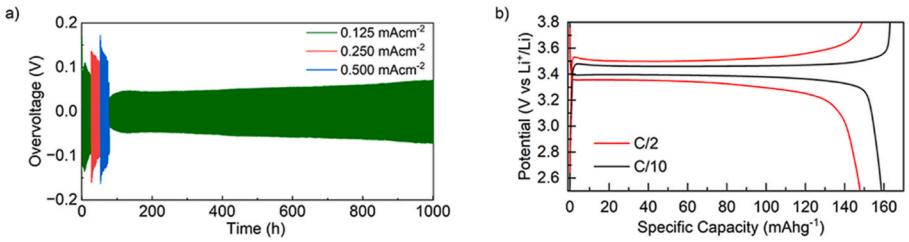

Fig. 7. a) Li//Li symmetric cell voltage profiles in LP30 at 30 °C using SA/PEO separator; b) Li//LFP cell voltage profiles using SA/PEO separator.

cycling stability of the CA/PEOaq, as shown in Fig. 8a that shows the capacitance retention (CR) and coulombic efficiency (CE) over 250,000 cycles. Capacitance retention was evaluated as the ratio of the discharge capacitance at a given cycle to that of the first cycle at each current density. As expected, the capacitance at 1 A g^{-1} was higher than that at 5 A g^{-1}, with the latter being 83 % of the initial value at 1 A g^{-1}. Remarkably, the capacitance retention resulted to be higher than the 90 % after 100,000 cycles at 1 A g^{-1} and around the 89 % after additional 150,000 cycles at 5 A g^{-1}, highlighting the stability of the separator in the supercapacitor configuration. The stability of the supercapacitor in an aqueous environment and its ability to operate at high specific current are also proven by the typical triangular shape of the charge-discharge curves in Fig. 8b, along with a relatively small ohmic drop, attributed to the low resistivity of the separator. In order to have information on the ability of the separator to limit the self-discharge of the supercapacitor, leakage current (I_{LEAK}) and self-discharge tests were performed in agreement with the FreedomCAR Ultracapacitor Test Manual [36]. The protocol consists of a galvanostatic charge at 5C up to a V_0 that is held over 72 h, followed by 72 h rest and, hence, discharge at the same current as the charge. The I_{LEAK} normalized to the discharge capacitance C_{RCT} (I'_{LEAK}) is shown in Fig. 8d. C_{RCT} has been obtained following the procedure reported in the Supplementary materials. The analysis of the cell voltage over time under rest conditions provided the self-discharge energy loss factor (SDLF), defined as the ratio of the energy lost over time to the maximum energy deliverable at the beginning of rest. SDLF was calculated by.

$$SDLF(t) = 1 - \left(\frac{V_t}{V_0}\right)^2 \tag{4}$$

where V_0 and V_t are the voltage at the beginning and at the time t, respectively. The SDLF curve over time is shown in Fig. 8c. I_{LEAK} and SDLF are critical parameters for evaluating the performance of a supercapacitor, and they are mainly affected by the electrolyte and by the overall reactivity of the interface electrode/separator/electrolyte. Hence, this separator provides a physically and chemically stable contact with the electrodes and minimizes self-discharge. An effective separator should provide excellent insulation between the electrodes, preventing any unintended conductive pathways that could lead to ohmic leakage. High leakage currents could arise because of poor separator integrity, defects, shrinkage, or insufficient ionic selectivity, which can significantly reduce the efficiency and lifespan of the device [37]. The I_{LEAK} was used to calculate the leakage resistances (R_p) by.

$$R_P = \frac{V_0}{I_{LEAK}} \tag{5}$$

The supercapacitor exhibits excellent performance and stability. The leakage current after 72 h is 11.54 μA F^{-1}, meaning the device retains charge efficiently with minimal energy loss. The leakage resistance (R_p) is 11.23 kΩ cm^2, indicating strong internal insulation and low self-discharge, which contributes to long-term charge retention. Additionally, the rest time required for the SDLF to drop below 0.1 is just 27.13 min, showing that the supercapacitor stabilizes rapidly after cycling.

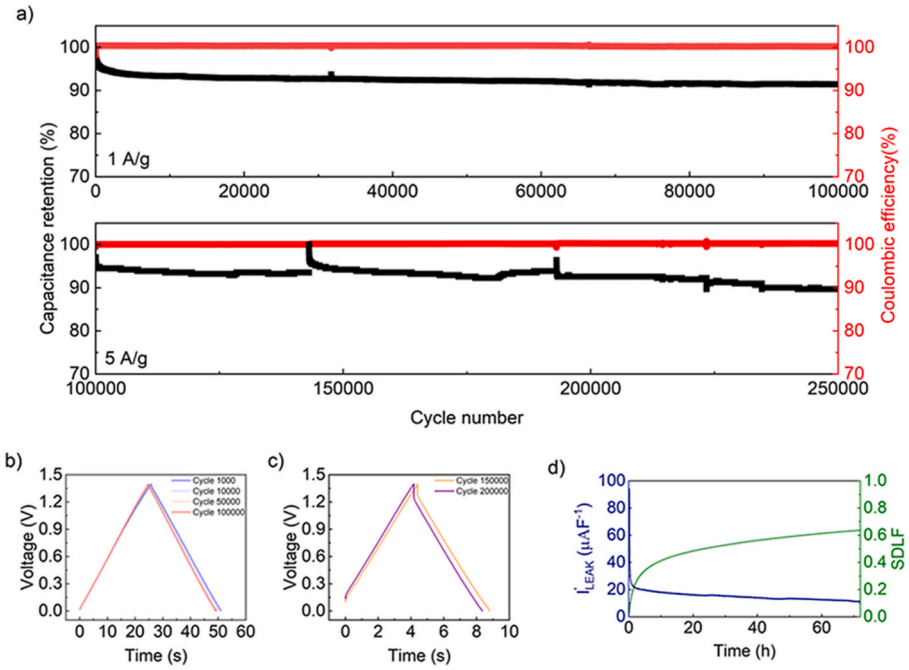

Fig. 8. (a) CR, CE of the AC symmetric supercapacitor with the CA/PEOaq separator over 250,000 cycles. Discontinuities are due to cycling interruptions; (b, c) voltage profiles at different cycle numbers, (d) I'_{LEAK} and SDLF over 72 h rest.

Overall, these parameters confirm that the supercapacitor is highly efficient, stable over time, and suitable for demanding, high-performance applications.

4. Conclusions

This study highlights the feasibility of alginate-based composites as sustainable and efficient separators for both lithium batteries and aqueous supercapacitors. Two novel separator designs were developed using an eco-friendly phase inversion process with water and ethanol as the primary solvents. The first separator, based on SA/PEO, demonstrated high stability in organic electrolyte environments, and the second, CA/PEO with an electrospun PVDF/PEO scaffold, showed enhanced mechanical strength and superior compatibility with aqueous electrolytes. The phase inversion process led to the suppression of the crystallinity of PEO, which is beneficial for ionic transport. Moreover, fine-tuning the separator fabrication resulted in higher electrolyte affinity compared to commercial analogues. Electrochemical tests proved the robustness of the SA/PEO separator in the presence of lithium metal, as proved by the Li//Li symmetric cells over extended cycling at different current densities. However, despite these encouraging results, SA/PEO separator tests in Li//LFP cells evidenced that in full cell configuration there could be some hindrance due to the limited source of Li ion in LFP, which deserves further investigations. On the contrary, outstanding stability (more than 250,000 cycles) and low leakage current (<12 μA F^{-1}) underscore the viability of alginate-based separators as environmentally friendly alternatives in aqueous supercapacitors. Their promising electrochemical performance, thermal stability, and sustainable production process make them attractive candidates for next-generation energy storage devices, bridging the gap between high performance and green chemistry principles.

CRediT authorship contribution statement

Antonio De Marco: Writing – review & editing, Writing – original draft, Validation, Investigation, Data curation, Conceptualization. **Giampaolo Lacarbonara:** Writing – review & editing, Validation, Supervision, Investigation, Data curation. **Mariangela Rea:** Writing – original draft, Validation, Investigation, Data curation. **Serena Tombolesi:** Validation, Investigation, Data curation. **Rossella Petruzzelli:** Writing – review & editing, Validation, Investigation, Data curation. **Chiara Gualandi:** Writing – review & editing, Supervision, Resources. **Maria Letizia Focarete:** Writing – review & editing, Supervision, Resources. **Catia Arbizzani:** Writing – review & editing, Supervision, Resources, Project administration, Funding acquisition, Conceptualization.

Declaration of competing interest

C.A. is Editor of the Journal. Given her role as editor, C.A. had no involvement in the peer review of this article and had no access to information regarding its peer review. Full responsibility for the editorial process for this article was delegated to another journal editor.

All the authors declare that they have no known competing financial interests or personal relationships that could have appeared to influence the work reported in this paper.

Acknowledgments

Work funded by European Union - Next Generation EU – NRRP (National Resistance and Resiliance Plan), Mission 4 Component 2 Investment 1.4 – Project CN_00000023 Sustainable Mobility Center (CN MOST, Spoke 13) and Investment 1.3 Project PE2 CUP J33C22002890007 Network 4 Energy Sustainable Transition (PE2 NEST, Spoke 6 Energy Storage).

Appendix A. Supplementary data

Supplementary data to this article can be found online at https://doi.org/10.1016/j.jpowsour.2025.238505.

Data availability

Data will be made available on request.

References

[1] Y. Gao, Z. Pan, J. Sun, Z. Liu, J. Wang, High-energy batteries: beyond lithium-ion and their long road to commercialisation, Nano-Micro Lett. 14 (2022) 94.
[2] S. Sharma, P. Chand, Supercapacitor and electrochemical techniques: a brief review, Results Chem. 5 (2023) 100885.
[3] N. Lingappan, W. Lee, S. Passerini, M. Pecht, A comprehensive review of separator membranes in lithium-ion batteries, Renew. Sustain. Energy Rev. 187 (2023) 113726.
[4] S. Zhang, A review on the separators of liquid electrolyte Li-ion batteries, J. Power Sources 164 (2007) 351–364.
[5] C. Orendorff, The role of separators in lithium-ion cell safety, Electrochem. Soc. Interface 21 (2012) 61.
[6] D.V. Horváth, R. Tian, C. Gabbett, V. Nicolosi, J.N. Coleman, Quantifying the effect of separator thickness on rate performance in lithium-ion batteries, J. Electrochem. Soc. 169 (2022) 030503.
[7] J. Cannarella, X. Liu, C.Z. Leng, P.D. Sinko, G.Y. Gor, C.B. Arnold, Mechanical properties of a battery separator under compression and tension, J. Electrochem. Soc. 161 (11) (2014) F3117–F3122.
[8] D.R.R. Kannan, P.K. Terala, P.L. Moss, M.H. Weatherspoon, Analysis of the separator thickness and porosity on the performance of lithium-ion batteries, Int. J. Electrochem. Sci. (2018) 1925708.
[9] A. Terella, F. De Giorgio, M. Rahmanipour, L. Malavolta, E. Paolasini, D. Fabiani, M.L. Focarete, C. Arbizzani, Functional separators for the batteries of the future, J. Power Sources 449 (2020) 227556.
[10] S. Zhong, B. Yuan, Z. Guang, D. Chen, Q. Li, L. Dong, Y. Ji, Y. Dong, J. Han, W. He, Recent progress in thin separators for upgraded lithium ion batteries, Energy Storage Mater. 41 (2021) 805841.
[11] S. Orangi, N. Manjong, D. Perez Clos, L. Usai, O. Stokke Burheim, A. Hammer Strømman, Historical and prospective lithium-ion battery cost trajectories from a bottom-up production modeling perspective, J. Energy Storage 76 (2024) 109800.
[12] S. Luiso, P. Fedkiw, Lithium-ion battery separators: recent developments and state of art, Curr. Opin. Electrochem. 20 (2020) 99–107.
[13] V. Deimede, C. Elmasides, Separators for lithium-ion batteries: a review on the production processes and recent developments, Energy Technol. 3 (2015) 453–468.
[14] M. Mulder, Phase inversion membranes, in: L. Rozelle, J. Cadotte, R. Corneliussen, E. Erickson, K. Cobian, C. Kopp (Eds.), Encyclopedia of Separation Science, Academic Press, Cambridge, MA, USA, 2000, pp. 3331–3346.
[15] Y. Liao, W. Li, Chapter 4 - separators for lithium-ion batteries, in: S. Thomas, D. Rouxel, N. Kalarikkal, B. Kottathodi, H.J. Maria (Eds.), Adv. Mater. Battery Sep. (2024) 73–140.
[16] S. Li, S. Pang, X. Qian, L. Jin, X. Shen, Enhancing the electrochemical properties of a lithium–sulfur battery using a modified separator with a phase-inversion layer, Dalton Trans. 53 (2024) 2937–2948.
[17] W. Schlemmer, J. Selinger, M.A. Hobisch, S. Spirk, Polysaccharides for sustainable energy storage – a review, Carbohydr. Polym. 265 (2021) 118063.
[18] M. Morales-Jiménez, D.A. Palacio, M. Palencia, M.F. Meléndrez, B.L. Rivas, Bio-based polymeric membranes: development and environmental applications, Membranes 13 (2023) 625.
[19] H. Kim, V. Guccini, H. Lu, G. Salazar-Alvarez, G. Lindbergh, A. Cornell, Lithium ion battery separators based on carboxylated cellulose nanofibers from wood, ACS Appl. Energy Mater. 2 (2) (2019) 1241–1250.
[20] J.P. Serra, A. Fidalgo-Marijuan, J. Teixeira, L. Hilliou, R. Gonçalves, K. Urtiaga, A. Gutiérrez-Pardo, F. Aguesse, S. Lanceros-Mendez, C.M. Costa, Sustainable lithium-ion battery separator membranes based on Carrageenan biopolymer, Adv. Sustain. Syst. 6 (12) (2022) 2200279.
[21] J. Jeong, J. Lee, J. Kim, J. Chun, D.G. Kang, S.M. Han, C. Jo, J. Lee, A biopolymer-based functional separator for stable Li metal batteries with an additive-free commercial electrolyte, J. Mater. Chem. A 9 (2021) 7774–7781.
[22] M. Hikam, P.P.P. Asri, F.H. Hamid, A.M. Anwar, M. Nasir, A. Sumboja, L.A.T. W. Asri, Electrospun poly(vinyl Alcohol)/Chitin nanofiber membrane as a sustainable lithium-ion battery separator, Langmuir 41 (1) (2025) 231–241.
[23] P. Sheth, D. Patil, B. Kandasubramanian, N. Mayilswamy, Advancements in chitosan membranes for promising secondary batteries, Polym. Bull. 81 (2024) 15319–15348.
[24] H. Hecht, S. Srebnik, Structural characterization of sodium alginate and calcium alginate, Biomacromolecules 17 (2016) 2160–2167.
[25] G. Lacarbonara, C. Arbizzani, S. Chini, S. Ratso, I. Kruusenberg, Graphitic carbon from CO_2 for sustainable li ion battery anodes, Mater. Adv. 3 (2022) 7087–7097.
[26] B. Dong, H. Zhu, X. Cai, C. Guo, Y. Hao, L. Xi, Rational design of alginate-derived network binder for high-performance silicon-based anodes in Li-ion batteries, J. Power Sources 626 (2025) 235745.

[27] C. Toigo, C. Arbizzani, K.-H. Pettinger, M. Biso, Study on different water-based binders for $Li_4Ti_5O_{12}$ electrodes, Molecules 25 (10) (2020) 2443.
[28] F. Bigoni, F. De Giorgio, F. Soavi, C. Arbizzani, Sodium alginate: a water-processable binder in high-voltage, cathode formulations, J. Electrochem. Soc. 164 (1) (2017) A6171–A6177.
[29] M. Ryou, S. Hong, M. Winter, H. Lee, J.W. Choi, Improved cycle lives of $LiMn_2O_4$ cathodes in lithium ion batteries by an alginate biopolymer from seaweed, J. Mater. Chem. A 1 (2013) 15224–15229.
[30] P. Chen, A. Chen, G. Li, Z. Yang, Y. Liu, Q. Zeng, L. Zhang, Paper-supported sodium alginate composite separator prepared by polymer-assisted phase separation for lithium ion batteries, ACS Sustainable Chem. Eng. 12 (2024) 16733–16743.
[31] A. La Monaca, F. De Giorgio, M.L. Focarete, D. Fabiani, M. Zaccaria, C. Arbizzani, Polyvinylidene difluoride–polyethyleneoxide blends for electrospun separators in Li-Ion batteries, J. Electrochem. Soc. 164 (1) (2017) A6431–A6439.
[32] S. Tombolesi, N. Zanieri, L. Bargnesi, M. Mernini, G. Lacarbonara, C. Arbizzani, A sustainable gel polymer electrolyte for solid-state electrochemical devices, Polymers 15 (14) (2025) 3087.
[33] F. Bossard, N. El Kissi, A. D'Aprea, F. Alloin, J.Y. Sanchez, A. Dufresne, Influence of dispersion procedure on rheological properties of aqueous solutions of high molecular weight PEO, Rheol. Acta 49 (2010) 529–540.
[34] M. Varma-Nair, B. Wunderlich, Heat capacity and other thermodynamic properties of linear macromolecules X. Update of the ATHAS 1980 data Bank, J. Phys. Chem. Ref. Data 20 (1991) 349–404.
[35] D. Di Cillo, L. Bargnesi, G. Lacarbonara, C. Arbizzani, Ammonium and tetraalkylammonium salts as Additives for Li metal electrodes, Batteries 9 (2) (2023) 142.
[36] F. Soavi, C. Arbizzani, M. Mastragostino, Leakage currents and self-discharge of ionic liquid-based supercapacitors, J. Appl. Electrochem. 44 (2014) 491–496.
[37] M. Haque, Q. Li, A.D. Smith, V. Kuzmenko, P. Rudquist, P. Lundgren, P. Enoksson, Self-discharge and leakage current mitigation of neutral aqueous-based supercapacitor by means of liquid crystal additive, J. Power Sources 453 (2020) 227897.